

One-Step Synthesis of Bunsenite Cadmium Oxide Nanoparticles

Essam M. Banoqitah ^{1,2,*} , Muneer Aziz Saleh ³, Mohammed M. Damoom ^{1,2} , Abdulsalam M. Alhawsawi ^{1,2} , Rafiziana Md. Kasmani ⁴  and Naif Mohammed Al-Hada ^{5,6,*} 

- ¹ Department of Nuclear Engineering, Faculty of Engineering, King Abdulaziz University, P.O. Box 80204, Jeddah 21589, Saudi Arabia
- ² Center for Training & Radiation Prevention, King Abdulaziz University, P.O. Box 80204, Jeddah 21589, Saudi Arabia
- ³ Office of Radiation Protection, Environmental Public Health, Washington State Department of Health, Richland, WA 99352, USA
- ⁴ School of Chemical and Energy Engineering, Universiti Teknologi Malaysia, Skudai, Johor Bahru 81310, Malaysia
- ⁵ Shandong Key Laboratory of Biophysics, Institute of Biophysics, Dezhou University, Dezhou 253023, China
- ⁶ Electronics and Communication Engineering Department, Faculty of Electrical and Electronics Engineering, Istanbul Technical University, 34467 Sariyer, Turkey
- * Correspondence: ebanqitah@kau.edu.sa (E.M.B.); naifalhada@yahoo.com (N.M.A.-H.)

Abstract: The present study proposes a simple synthesis technique for producing bunsenite cadmium oxide nanoparticles. A variety of techniques were used to determine the structure, morphology, elemental content, and optical properties of bunsenite cadmium oxide nanoparticles. The samples' XRD spectra at 500 °C and above confirmed the presence of cubic bunsenite and cadmium oxide structures. The crystallite size was increased from 29 nm to 62 nm as the calcined temperature increased from 500 °C to 800 °C. The dispersion of the particles of bunsenite cadmium oxide improved with an increasing calcination temperature. An equivalent increasing trend was indicated by the mean grain size displayed via field emission scanning electron microscopy (FESEM) micrographs. Furthermore, the UV-Vis spectra showed that multiple energy band gaps attenuated as the calcination temperature increased. The mean particle size, as measured by transmission electron micrographs, appeared to increase in tandem with the calcination temperature. The obtained bunsenite and cadmium oxide nanoparticles have potential for employment in a wide range of semiconductor applications.

Keywords: bunsenite cadmium oxide nanoparticles; polyvinylpyrrolidone; thermal technique



Citation: Banoqitah, E.M.; Saleh, M.A.; Damoom, M.M.; Alhawsawi, A.M.; Kasmani, R.M.; Al-Hada, N.M. One-Step Synthesis of Bunsenite Cadmium Oxide Nanoparticles. *Appl. Sci.* **2023**, *13*, 438. <https://doi.org/10.3390/app13010438>

Academic Editor: Fabrice Goubard

Received: 18 November 2022

Revised: 23 December 2022

Accepted: 26 December 2022

Published: 29 December 2022



Copyright: © 2022 by the authors. Licensee MDPI, Basel, Switzerland. This article is an open access article distributed under the terms and conditions of the Creative Commons Attribution (CC BY) license (<https://creativecommons.org/licenses/by/4.0/>).

1. Introduction

Transition metal oxide nanoparticles have unique structural, optical, magnetic, and electrical properties that allow them to have small crystallite sizes, large surface areas, and quantum dimensions [1,2]. These nanoparticles have lately been exploited in biological, physical, chemical, and electrical applications as a result of their properties [3–6]. Cadmium oxide (CdO) is an n-type semiconductor with a direct bandgap ranging from 2.2 to 2.5 eV and an indirect bandgap ranging from 1.36 to 1.98 eV [7–9]. It is very electrically conductive, has a high carrier concentration, is highly chemically stable, widely available, highly transparent in the visible electromagnetic spectrum region, and is relatively inexpensive [10,11]. Consequently, it is compatible with many applications, including solar cells, photodiodes, photoresistors, photosensors, and transparent electrodes [12–14]. A semiconductor of the p-type, bunsenite (NiO) has a broad bandgap between 3.6 and 4.0 eV [15–18]. Its electronic, magnetic, chemical, and electrical properties [19–21] make it appropriate for catalysis, the storage of energy, and conversion in many applications [20,22–24].

The properties of distinct individual oxides have been improved by combining multiple metal oxides to form innovative nanocomposites for usage in a variety of applications [25–27]. Because of parameters such as chemical composition, crystallite size, and constituent phase volume, the physical properties of the nanocomposites differ from those of bulk materials [28–35]. Additionally, nanocomposites may have features that complement

one another. For example, several band gaps can form from both oxide semiconductors, which may or may not share properties with the constituents of individual metal and metal oxide nanoparticles [36–38]. As a result, a composite arising from the suitable integration of bunsenite cadmium oxide nanoparticles and other metal oxides could potentially boost photocatalytic activity [25,39,40]. However, there are some advantages to using a thermal treatment strategy to synthesize bunsenite cadmium oxide nanocomposites, such as scalability, product stability, low cost, and ease of handling. Because it is capable of absorbing specific solar energy wavelengths, this approach enables exact particle size control and great purity, making it perfect for use in solar cell energy applications.

Bunsenite and cadmium oxide nanoparticles have been produced using a simple thermal treatment approach. This process does not necessitate the use of hazardous chemicals, does not generate hazardous waste, and does not flush hazardous materials down the drain [27]. In this study, a bunsenite cadmium oxide nanoparticle was synthesized using nickel nitrate, deionized water, cadmium nitrate, and polyvinylpyrrolidone (PVP). Thermogravimetric analysis (TGA), X-ray diffraction (XRD), field emission scanning electron microscopy (FESEM), energy dispersive X-ray (EDX) scanning, Fourier transform infrared (FTIR) spectroscopy, and UV-Vis were used to characterize the prepared samples.

2. Materials and Methods

2.1. Materials

As precursors, nickel nitrate ($\text{Ni}(\text{NO}_3)_2 \cdot 6\text{H}_2\text{O}$) metallic salt and cadmium nitrate ($\text{Cd}(\text{NO}_3)_2 \cdot 4\text{H}_2\text{O}$) salt were used. Polyvinyl pyrrolidone (PVP) was employed as a capping agent, and deionized water was used as a solvent to disperse the nanoparticles. Sigma-Aldrich provided all chemical ingredients, including $\text{Ni}(\text{NO}_3)_2 \cdot 6\text{H}_2\text{O}$, $\text{Cd}(\text{NO}_3)_2 \cdot 4\text{H}_2\text{O}$, and PVP, which were all 99 percent pure.

2.2. Methodology

The process by which the bunsenite cadmium oxide nanoparticles were produced was used in several procedures. One procedure involved the dissolution of 0.4 mmol $\text{Ni}(\text{NO}_3)_2 \cdot 6\text{H}_2\text{O}$, 0.6 mmol $\text{Cd}(\text{NO}_3)_2 \cdot 4\text{H}_2\text{O}$ [4:6 of Ni to Cd] and 4 g of PVP, followed by vigorous mixing to produce a standardized solution. It was placed on a glass plate and exposed to 80 °C for 24 h to induce dehydration in the latter. Pulverization of the sample was the next step. Temperatures ranged from 500 to 800 °C for four independent samples, which were then subjected to XRD and FTIR investigations at 30 °C for a portion of the sample set aside for these tests.

2.3. Characterization

To analyze the prepared samples produced in the method described here, a variety of characterization techniques were used. A Perkin Elmer thermogravimetric analyzer was used for thermal analysis. The parameters of analysis included nitrogen as a purging gas, a heating rate of 10 °C/minute, and a temperature range of 30–900 °C. A Shimadzu 6000 X-ray diffractometer was used to analyze the samples' crystalline structure. Furthermore, CuK (0.154 nm) was employed as the radiation source to produce diffraction patterns at temperatures ranging from 20 to 80 degrees Celsius. An FESEM was used to investigate the consistency and morphology of the nanoparticles, while an EDX spectrometer was utilized to study the elemental composition of the samples, which had been coated with gold before being studied with an EDX spectrometer. The samples' infrared spectra (280–4000 cm^{-1}) were analyzed using a KBr-based Fourier transform infrared (FTIR) spectrometer (Perkin Elmer 1650 model). This allowed us to assess whether an inorganic sample composite was present after calcination and ensure that the capping agent had been removed. Finally, the optical characteristics of the samples were studied at room temperature (200–800 nm) using a UV-visible spectrophotometer (Shimadzu UV-3600 model).

3. Results

3.1. Formation of Bunsenite Cadmium Oxide NPs

The interaction of the capping agent (PVP) with the Ni^{2+} and Cd^{2+} ions is depicted in Figure 1, which is held together by the strong ionic interactions generated between the metallic ions and the polymer chain amide groups. Metallic salts have been observed to dissolve in the presence of amide groups in pyrrolidone rings and methylene groups in polymers due to the constant advancement of electrostatic and steric stabilization while the sample is still in the solution stage. The metallic ions are frequently enclosed by shorter polymer chains after surface absorption [30,31,41–43], which probably arose initially due to some degree of crumbling in the PVP stabilizer. Short polymer chain capping allowed for the homogeneous scattering of metallic ions in the material's vacant spaces and networks. Furthermore, the calcination procedure, which oxidized Ni^{2+} and Cd^{2+} ions, led to the formation of bunsenite cadmium oxide nanoparticles. A solid-state interaction between NiO and CdO was initiated at high temperatures during the beginning of the metal phase growth, resulting in binary nanoparticles. During this step, organic components were removed, and the nanoparticles began to combine as a result of the action of higher calcination temperatures. Organic compound-containing gases, such as NO, N_2 , CO, or CO_2 , disintegrated during the subsequent calcining process. Furthermore, the other organic components were removed during the calcination stage, and the increased temperature causes fusion among the nanoparticles, increasing particle size while obtaining the lowest surface energy. The use of PVP has a purpose that extends beyond the solution and drying stages, as the nucleation of bunsenite cadmium oxide nanoparticles is stimulated throughout the calcination process. The formation of smaller nanoparticles was decreased due to the high molecular weight and the creation of repulsive forces by the polyvinyl groups. As a result, particles grew larger with lower surface energy. The PVP addition had an effect that extended beyond the solution and drying stages, as evidenced by its ability to enhance bunsenite cadmium oxide nanoparticle nucleation throughout the calcination process. Smaller nanoparticles grouped to a lesser amount when PVP was absent due to their high molecular weight and the electrostatic repulsion created by polyvinyl groups [21,44]. The capping agent action of PVP can have a considerable impact on the formation of bunsenite and cadmium oxide nanoparticles. PVP also regulates nanoparticle growth by capping them, decreasing the rate of accumulation, improving crystallinity, and assisting in the consistency of the prepared samples' characterization [41,45].

3.2. TGA Analysis

PVP and bimetal nitrate were thermally examined through thermogravimetric (TGA) analysis, which also helped to determine the ideal temperature at which the process of calcination should start. Figure 2 depicts the TGA curve correlated with the generated compound containing PVP and bimetallic nitrates prior to calcination. Weight loss occurred in three stages following calcination. The first phase appeared at temperatures less than $160\text{ }^\circ\text{C}$ and was thought to be caused by moisture trapped in the sample. Meanwhile, the minor peak at $393\text{ }^\circ\text{C}$ was attributed to the breakdown of NO_x molecules [33]. At $452\text{ }^\circ\text{C}$, the majority of the PVP content was broken down and a significant quantity of weight was lost. The weight loss as a function of temperature became insignificant at $494\text{ }^\circ\text{C}$ because the remaining polymer composition had been converted into carbonaceous yields [34], and no additional weight was lost at temperatures above $496\text{ }^\circ\text{C}$ because the carbonaceous material had indeed been eliminated from either sample in the temperature range $438\text{--}488\text{ }^\circ\text{C}$ [46].

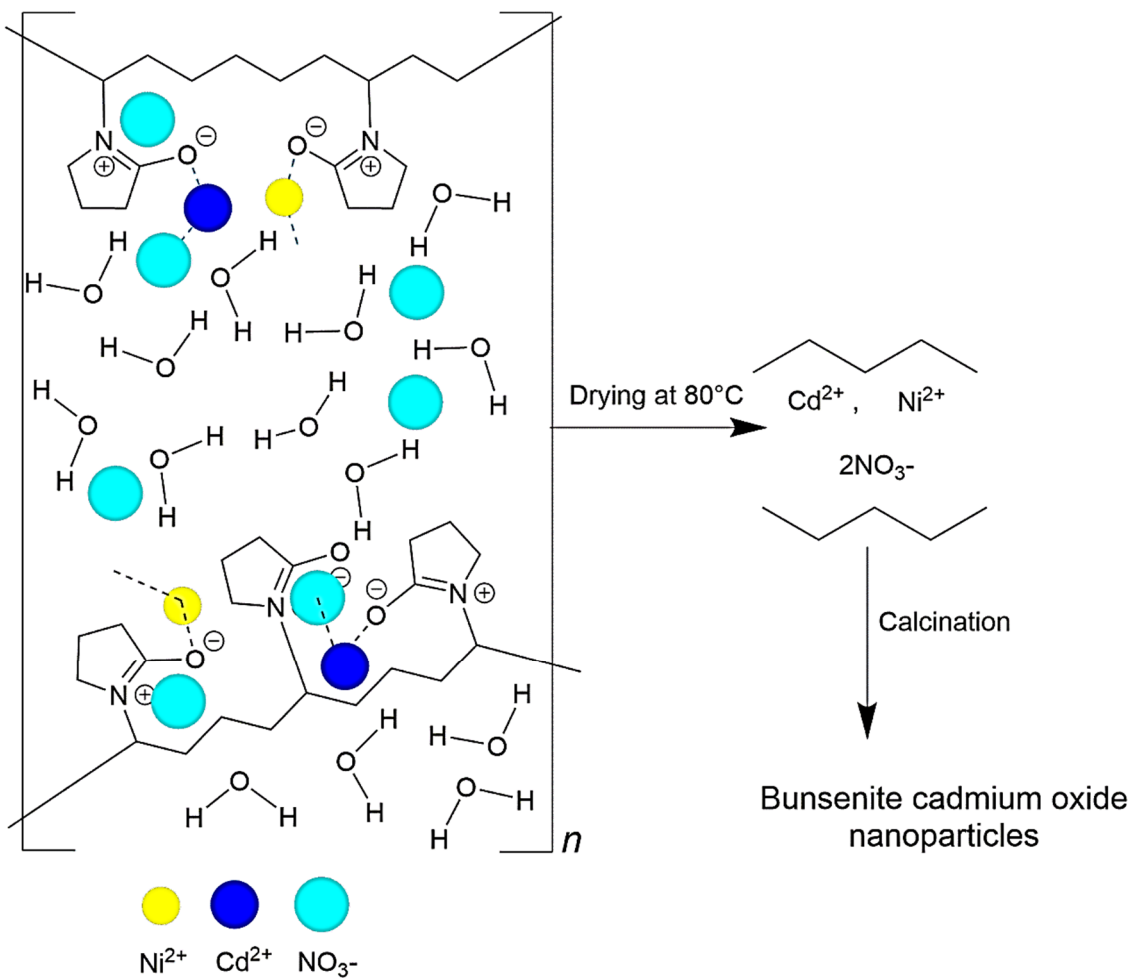


Figure 1. Proposed diagram graphic of the formation of bunsenite cadmium oxide nanoparticles (NPs) [33].

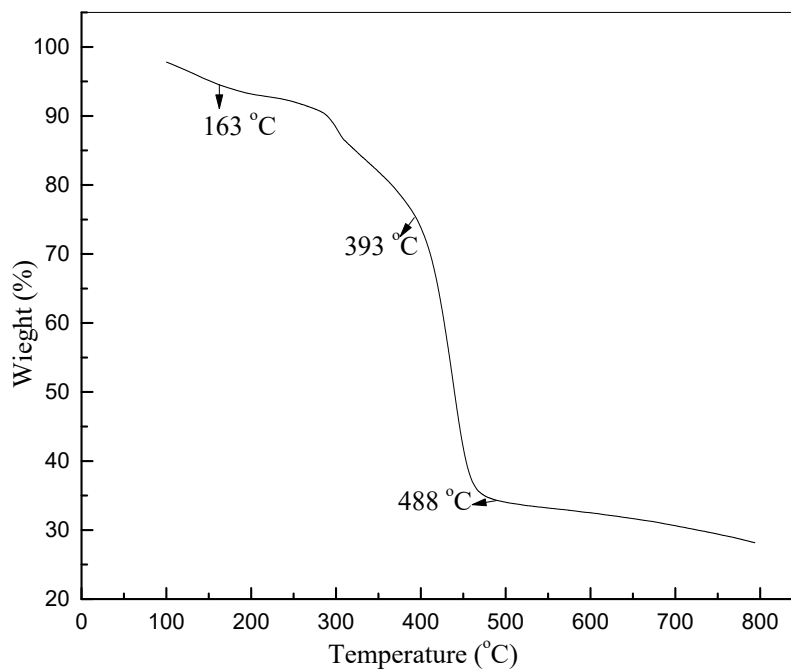


Figure 2. Thermogravimetric analysis (TGA) curve for bimetallic nitrates and PVP.

3.3. Structural Analysis

After drying at 80 °C, nickel nitrate, cadmium nitrate, and PVP content were analyzed. Because no diffraction peaks were observed in Figure 3a, it was concluded that the sample remained amorphous prior to calcination. Figure 3 depicts the XRD patterns associated with the samples that were calcined at room temperature, 500, 600, 700, and 800 °C. The diffraction peaks for CdO and NiO nanoparticles were marked by a star and a sharp, respectively, in the samples that had been calcined. The cadmium oxide nanoparticles' diffraction peaks corresponded to (111), (002), (022), (113), and (222), and the plane signs have been identified at 2θ 33.70°, 38.50°, 55.26°, 65.50°, and 69.08°, respectively. Meanwhile, the bunsenite nanoparticles' diffraction peaks corresponded to (111), (002), (022), (113), and (222), and the plane signs have been identified at 2θ 37.02°, 43.20°, 62.29°, 75.34°, and 79.21°. The nanoparticles were equivalent to the standard card diffraction patterns associated with bunsenite oxide (JCPDS cards 36-1451 data) and cadmium oxide (PDF card No: 005-0640 data) [21,36]. Furthermore, given that the crystallite size parameters were established to increase as the temperature of calcination rose, the Scherrer formula (Formula (1)) was employed to determine the average crystallite size at all peaks. The full width of the half maximum broadening of the CdO and NiO peaks of the XRD patterns was applied to calculate the average crystallite size using the Scherrer formula:

$$D = 0.9 \lambda / \beta \cos \theta \quad (1)$$

In Formula (1), the crystallite size measured in nm is denoted by D , the entire width of the diffraction line at half of the maximum intensity measured in radians is denoted by β , the X-ray wavelength of Cu $K\alpha$ 0.154 nm is denoted by λ , and the Bragg angle is denoted by θ . Table 1 shows the calculation crystallite size of bunsenite cadmium oxide nanoparticles for each peak using the Scherrer formula at a temperature of 800 °C. Table 1 shows the crystallite size enlargement calculated with the Scherrer formula for the prepared samples calcined in ranging temperatures from 500 to 800 °C. The crystallite size increased in direct proportion to the increase in calcination temperature, which was ascribed to particle size enlargement. Furthermore, the sharper and narrower diffraction peaks with more intensity (Figure 3b–e) indicate that crystallinity was significantly improved. This is because the temperature of the calcination process was increased.

Table 1. XRD results of the prepared sample were calculated using diffraction peak by Scherrer formula at temperatures of 800 °C.

2 Theta	Sample	hkl	FWHM	Calculation of the Crystallite Size Using Scherrer Formula at Temperature 800 °C
33.70°	CdO	111	0.182	45
37.02°	NiO	111	0.184	67
38.50°	CdO	002	0.183	46
43.20°	NiO	002	0.137	62
55.26°	CdO	022	0.131	69
62.29°	NiO	022	0.163	56
65.50°	CdO	113	0.126	63
69.08°	CdO	222	0.143	67
75.34°	NiO	113	0.151	66
79.21°	NiO	222	0.130	79
Average				62

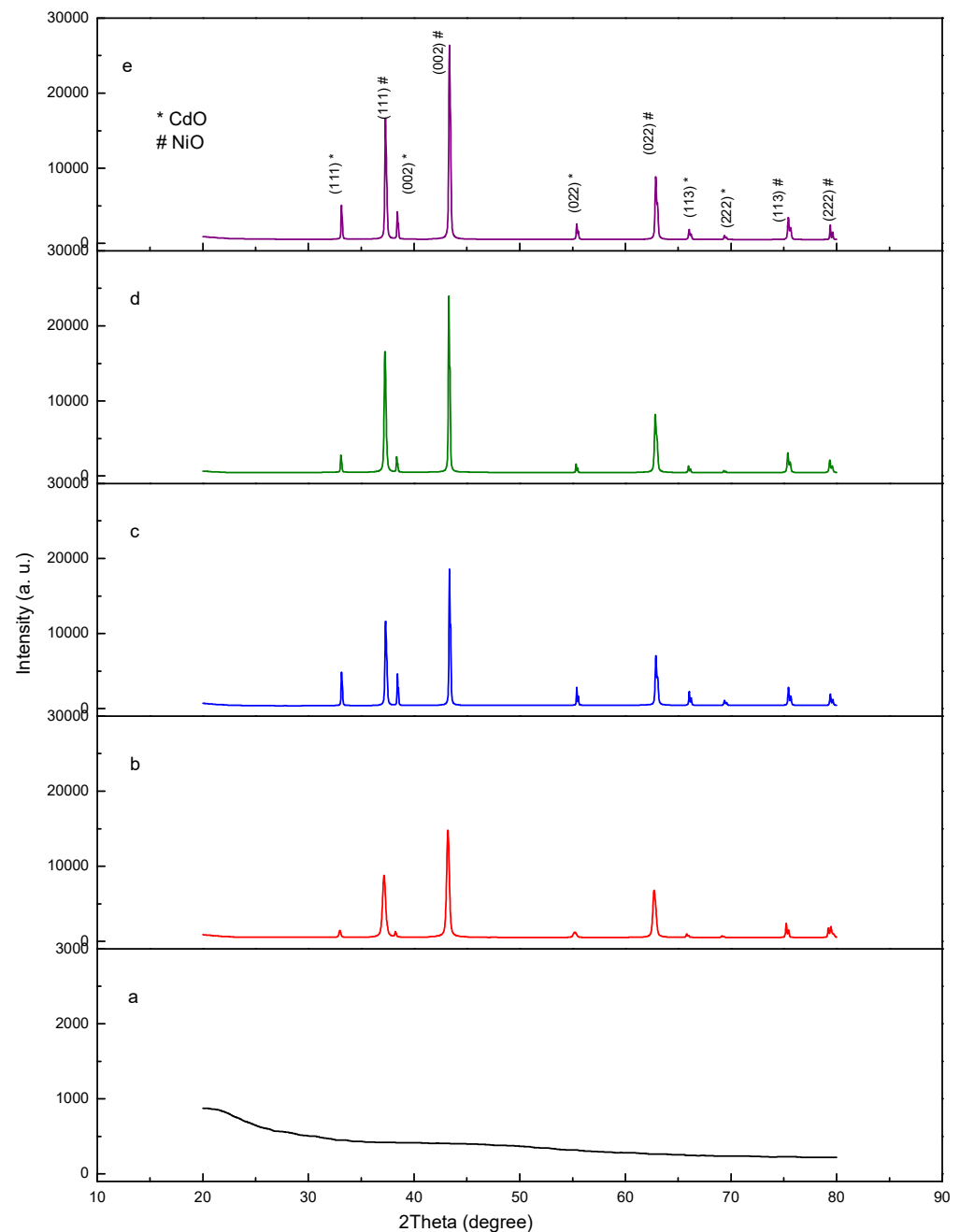


Figure 3. XRD results of the prepared samples in calcinations of (a) room temperature, (b) 500, (c) 600, (d) 700, and (e) 800 °C.

3.4. SEM Analysis

The morphology of the prepared samples was investigated via field emission scanning electron microscopy (FESEM) at temperatures between ambient temperature and 500–800 °C. Figure 4 shows micrographs associated with the bunsenite cadmium oxide nanoparticles at ambient temperatures of 500, 600, 700, and 800 °C. At room temperature, the sample exhibited a form that was neither homogenous nor regular (Figure 4a); however, at temperatures of 500 °C and higher, it assumed a form that was aggregated, spherical, and regular (Figure 4b,e) [21,36]. As the calcination temperature increases, the grains enlarged individually, so that the sample exhibited better distribution and uniformity (Figure 4c,d).

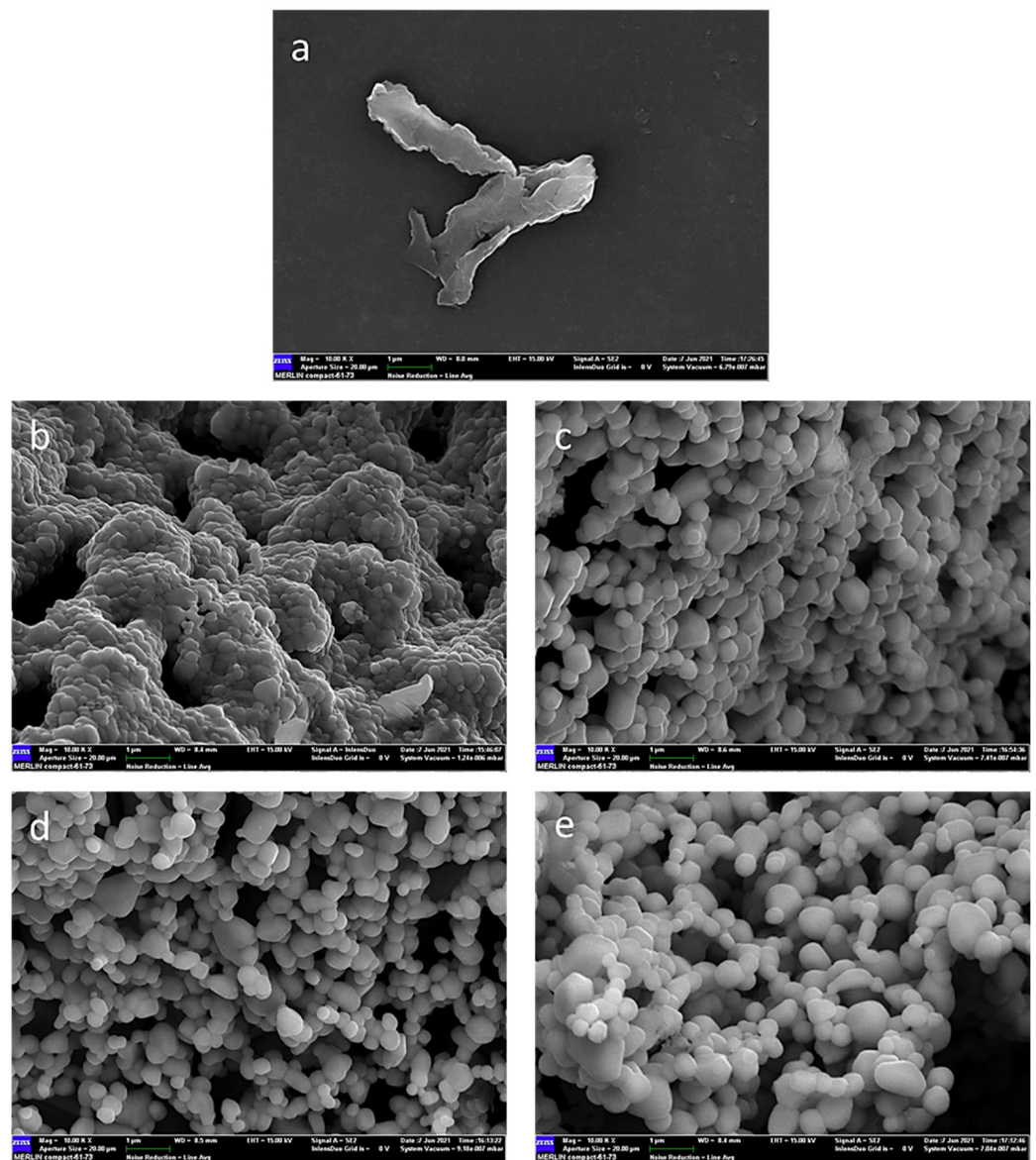


Figure 4. SEM images of prepared samples at temperatures of (a) room temperature, (b) 500, (c) 600, (d) 700, and (e) 800 °C.

3.5. EDX-Based Analysis of the Elemental Composition

Figure 5 illustrates the EDX spectra as well as the atomic composition of prepared samples synthesized at a temperature of 700 °C. The occurrence of corresponding nickel, cadmium, and oxygen peaks in the sputtered sample confirmed that bunsenite cadmium oxide nanoparticles were present. The [Ni:O] atomic composition, which was [20.10:19.20], and the [Cd:O] atomic composition, which was [30.67:30.03], were used to establish the 4:6 of Ni to Cd precursors, which was equivalent to their proportions in the chemical formula of bunsenite cadmium oxide. The peaks of Au shown in the spectrum were formed using the sputtering procedure of coating with gold, used during the preparation of the sample for EDX testing. The EDX analysis confirmed the presence of bunsenite cadmium oxide nanoparticles. The fact that no elements were lost during this process proved that the thermal treatment route was well controlled.

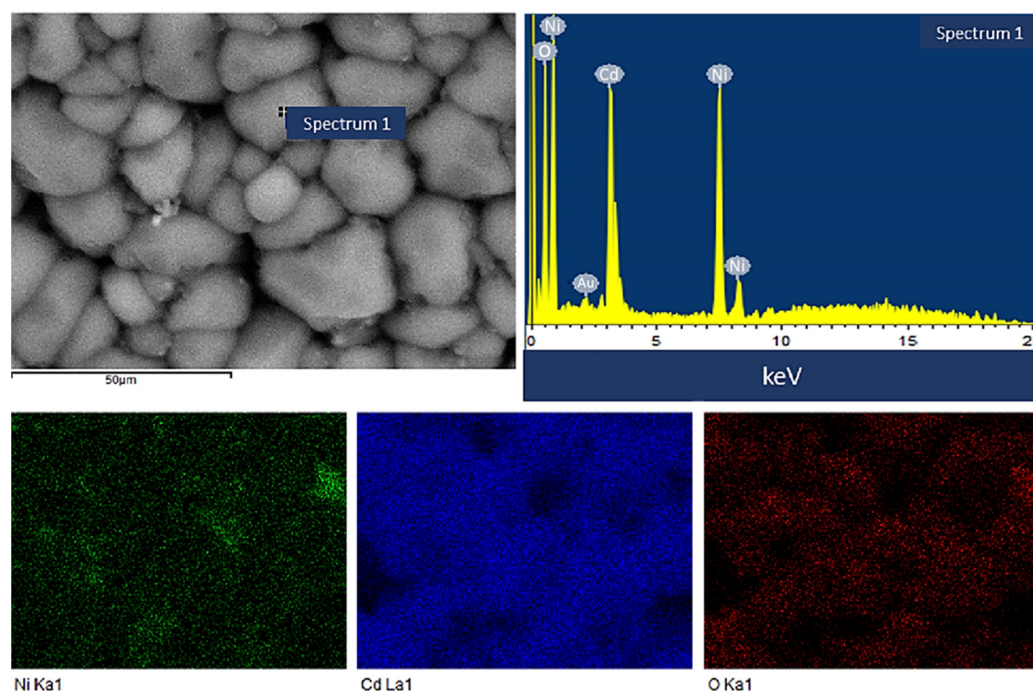


Figure 5. The EDX spectrum of the prepared sample was calcined at 700 °C.

3.6. FTIR-Based Analysis of Phase Composition

The sample FTIR spectra are illustrated in Figure 6 at (a) ambient temperature, (b) 500, (c) 600 (d) 700, and (e) 800 °C in the 280–4500 cm^{-1} range. Figure 6a also shows the absorption peaks for PVP and bimetal nitrate. N–H, C–H, and C=O stretching vibrations were identified as the sources of the absorption peaks at wavenumbers 3414, 2945, and 1646 cm^{-1} before calcination. It was considered that the absorption peaks at 1428 cm^{-1} and 1277 cm^{-1} were, respectively, caused by C–H bending vibration and C–N stretching vibration [41]. Furthermore, the bands that contained peaks at 839, 736, and 639 cm^{-1} were mapped to NO_3 groups, with the C–C ring and C–N=O bending being the cause of the vibrations. Meanwhile, Cd–OH band and Ni–OH vibrations were deemed to have caused the peaks at 582 and 608 cm^{-1} . Most broadband absorption disappears, as shown in Figure 6b–e for a calcined sample at 500 °C, except for absorption at 3404 cm^{-1} . For the samples at temperatures over 500 °C, the peaks at (447, 424, 413, 408) and (404, 396, 387, 374) cm^{-1} were assigned to the Ni–O and Cd–O bands, respectively. The two-fold absorption peak was attributed to quite pure sample nanoparticles, as evidenced by the verified shift in wave number for the product nanoparticles' spectra as calcination temperatures increased. This means that there are no other contaminants in the samples. Thus, the proposed technique of thermal treatment was validated to improve the crystallinity of synthesized bunsenite cadmium oxide nanoparticles.

3.7. UV-Visible Analysis

The diffuse reflectance spectra of bunsenite cadmium oxide nanoparticles were measured using a UV-visible spectrophotometer. Figure 7 shows the reflectance spectra of the produced samples that were calcined at various temperatures in a wavelength range of 220–800 nm. Regarding the two reflection peaks at around 357 nm and 625 nm, Figure 7 illustrates the Ni^{2+} and Cd^{2+} species identified in the prepared samples. These (357 nm and 625 nm) were assumed to be the origins of the reflection peaks at 340–400 and 625 nm. All of the samples also showed an absorption band at around 340–400 and 625 nm, which were assumed to be caused by a charge transfer transition from oxygen to metal. The presence of both Ni^{2+} and Cd^{2+} ions in all samples confirms the production of bunsenite cadmium oxide nanoparticles [21,33]. The relatively high intensity of the aforementioned peaks, as

well as the blue shift in their wavelengths, attested to this. The band at 589 nm indicated that Cd^{2+} was present in the samples and was caused by Cd^{2+} ions. This band was found in all of the prepared samples, regardless of the temperature they were calcined at [30].

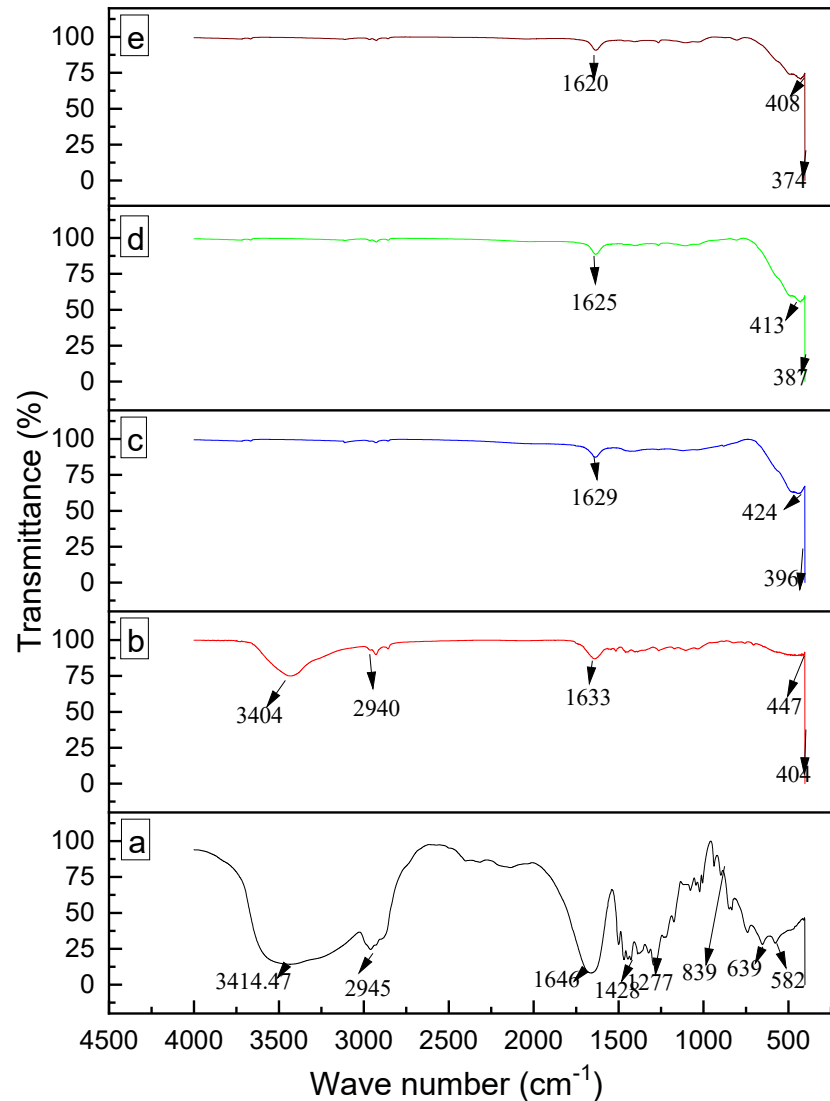


Figure 6. FTIR spectra of (a) PVP and bunsenite cadmium oxide at different temperatures: (a) room temperature, (b) 500, (c) 600, (d) 700, and (e) 800 °C.

An absorption broadband of between 340 and 625 nm was exhibited by every sample as well. This band was considered to originate from an $\text{O}^{2-}\text{Ni}^{2+}$ charge transfer transition. The confirmation that all samples contained both Ni^{2+} and Cd^{2+} ions validated the synthesis of bunsenite cadmium oxide. The results from Figure 7 were employed to determine the absorption coefficient from the Kubelka–Munk (KM) function based on Formula (2):

$$F(R_{\infty}) = (\alpha/S) = (1 - R_{\infty})/2R \quad (2)$$

In Formula (2), the absorption coefficient, scattering coefficient, and KM function are respectively signified by α , S , and $F(R_{\infty})$.

The KM function could be used instead of α for the diffused reflectance spectra to measure the optical absorption edge energy. It was observed that a plot of $F(R_{\infty}) E$ with E was linear near the edge for the direct allowed transition ($\eta = 1/2$). The value of that energy for the sample is indicated by the intercept of the line on the abscissa ($F(R_{\infty}) E = 0$) [9,33,47].

The Kubelka–Munk equation and reflectance spectra data were employed to determine the optical band gap for every sample subjected to calcination [48]:

$$(F(R_{\infty}) \cdot hv)^2 = (A(hv - E_g)) \quad (3)$$

In Formula (3), the apparent remission parameter or Kubelka–Munk function is denoted by $F(R_{\infty})$, the incident photon energy is denoted by hv , the constant given by the transition probability is denoted by A , and the diffuse reflectance derived from the R_{∞} that obtained from $R_{\infty} = R_{\text{sample}}/R_{\text{standard}}$ [49]. The mapped values of $(F(R_{\infty})hv)^2$ against hv are presented in Figure 6. The linear plot ranges with extrapolation to the (hv) axis were employed to determine the values of the optical bandgap of the prepared samples at various temperatures of calcination. Every sample subjected to calcination exhibited the two optical band gaps presented in Figure 8 and Table 2. The initial band gaps at 3.94, 3.83, 3.67, and 3.53 eV, respectively corresponding to the calcination temperatures of 500, 600, 700, and 800 °C, were explained by the presence of NiO nanoparticles in the samples. The bunsenite oxide electronic transition was interpreted as a direct step from oxygen to metal ns or np levels. Meanwhile, the second band gaps at 3.00, 2.96, 2.87, and 2.80 eV, respectively corresponding to the calcination temperatures of 500, 600, 700, and 800 °C, were explained by the occurrence of cadmium oxide nanoparticles in the samples. As the temperature of calcination and particle size increased, those energy band gaps were observed to become smaller [43]. This phenomenon could be explained by the quantum size effect [21,33]. This is due to a reduction in the band gaps between the valance and conduction bands for the d-shell electrons of Ni^{2+} and Cd^{2+} ions. This implies that transitions between these two bands could have occurred.

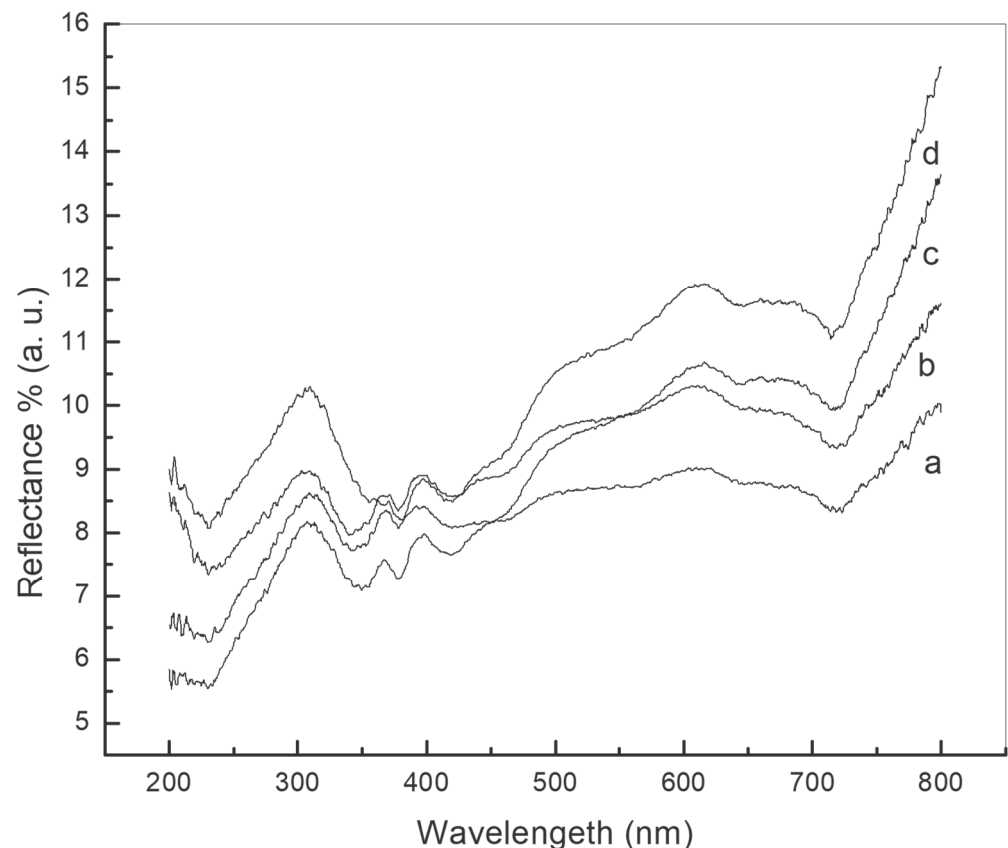
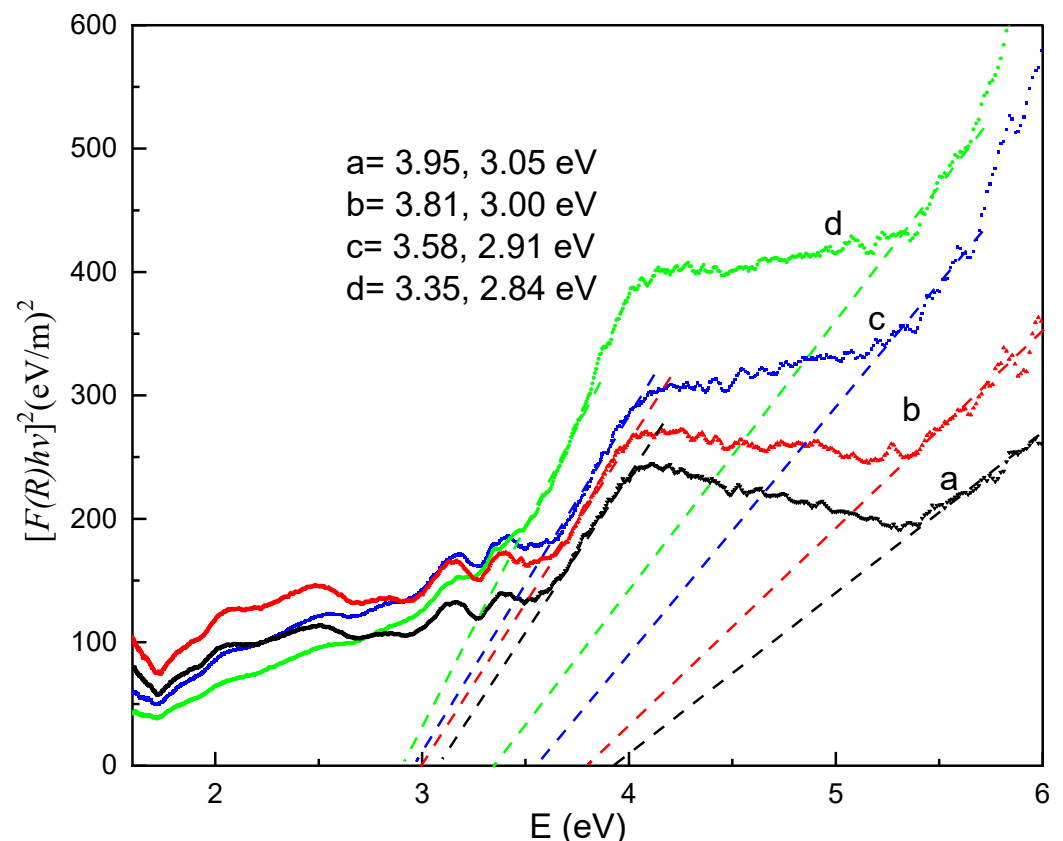


Figure 7. The reflectance of prepared samples at temperatures of (a) 500, (b) 600, (c) 700, and (d) 800 °C.

Table 2. Summary of calcination temperatures and bandgaps values.

T °C	500	600	700	800
(NiO) _x (CdO) _{1-x} Nanoparticles	Eg (eV)	Eg (eV)	Eg (eV)	Eg (eV)
(NiO) _{0.4}	3.95	3.81	3.58	3.35
(CdO) _{0.6}	3.05	3.00	2.91	2.84

**Figure 8.** The bandgaps values of prepared samples at temperatures of (a) 500, (b) 600, (c) 700, and (d) 800 °C.

3.8. Transmission Electron Microscopy (TEM) Analysis

The transmission electron microscopy (TEM) images of calcined bunsenite cadmium oxide nanoparticles at 500, 600, 700, and 800 °C (Figure 9a–d) reveal that all the produced samples exhibited homogeneous morphology. TEM images show that the particle sizes of the samples are consistently consistent throughout all temperature ranges measured by XRD and TEM. Increasing the calcination temperature resulted in larger particles (31, 44, 54, and 65 nm at temperatures of 500, 600, 700 and 800 °C, respectively), as expected; the smallest crystal size was obtained at 500 °C. Several nearby particles adhere to one another due to surface melting at higher temperatures, resulting in an increase in particle size. The nanoparticles of the bunsenite cadmium oxide were found to be spherical at all of the investigated calcination temperatures. Therefore, uniform bunsenite cadmium oxide nanoparticles have been produced by this thermal treatment method, with the presence of PVP acting as a restraint on the particle size via the reduction in agglomeration.

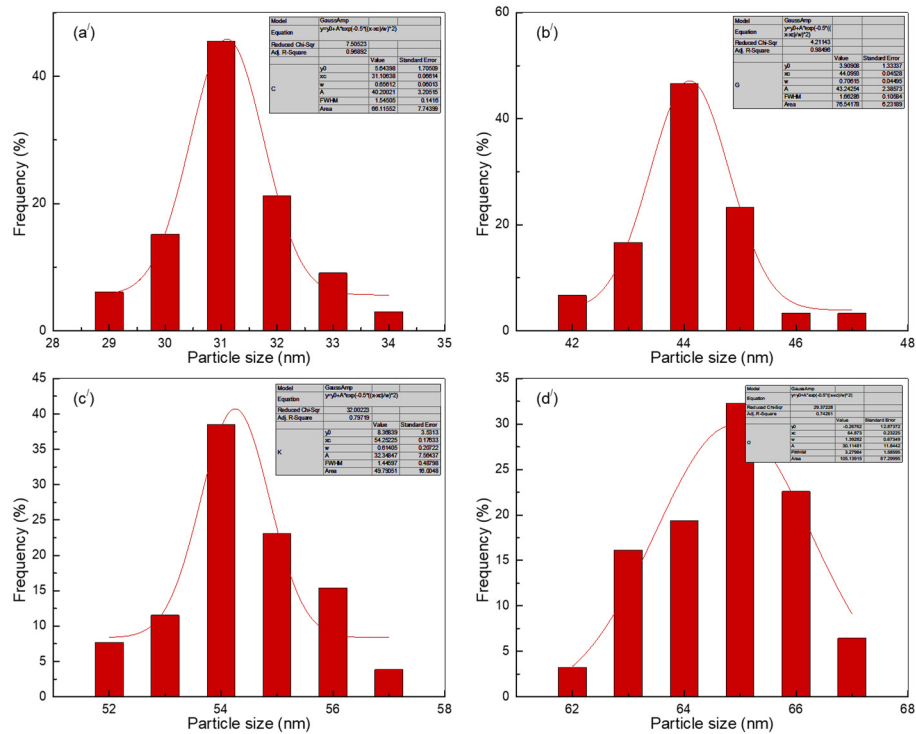
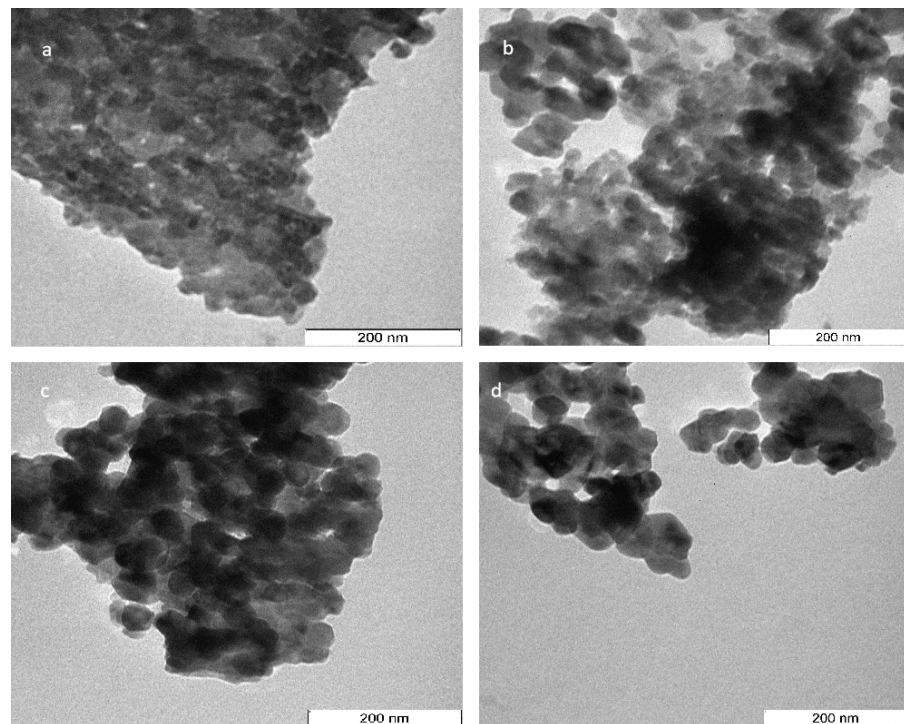


Figure 9. TEM images and particle size distribution of bunsenite cadmium oxide nanoparticles at (a,a') 500, (b,b') 600, (c,c') 700, and (d,d') 800 °C calcination temperatures.

4. Conclusions

The XRD analysis of the samples revealed that the proposed technique of thermal treatment generated nanocrystalline bunsenite cadmium oxide with face-centered cubic structures at every temperature of calcination that was employed. The crystallite size increased as temperature increased, from 29 nm at 500 °C to 62 nm at 800 °C. Furthermore,

the peaks associated with Ni, Cd, and O that were highlighted by EDX analysis validated the atomic composition of bunsenite and cadmium in proportions equivalent to those in the original mixture. The fact that no element was lost during synthesis and that bunsenite cadmium oxide nanoparticles were successfully produced demonstrated that the simple technique of thermal treatment was effective. The integration of metal oxide bands at every temperature of calcination was examined via FT-IR spectroscopy. In addition, an FTIR investigation was performed to verify the best temperature greater than 500 °C with which to remove organic compounds. This was observed to be pure bunsenite cadmium oxide nanoparticles formed at calcination temperatures of 500°C or higher. Moreover, as shown by the reflectance spectra, the bandgap energy of bunsenite cadmium oxide nanoparticles diminished as the calcination temperature rose. The mean particle size, as measured by transmission electron micrographs, appeared to increase in tandem with the calcination temperature. The results of this study indicate the proposed thermal treatment's viability as a simple and low-cost method for manufacturing extremely pure bunsenite cadmium oxide nanoparticles. The process is preferable to others because it does not use chemical reagents and has no environmental impacts. Furthermore, because the calcination temperature may be modified, the process makes it easier to produce semiconductor materials with more than one band gap. Because they can absorb particular wavelengths of solar energy, such materials are suitable for energy applications.

Author Contributions: Conceptualization, E.M.B., M.A.S., M.M.D., A.M.A., R.M.K. and N.M.A.-H.; methodology, E.M.B., M.A.S., M.M.D. and N.M.A.-H.; validation, E.M.B., M.A.S. and N.M.A.-H.; formal analysis, E.M.B., M.A.S., M.M.D., A.M.A., R.M.K. and N.M.A.-H.; investigation, E.M.B., M.A.S., M.M.D. and N.M.A.-H.; resources, E.M.B., M.A.S., M.M.D., A.M.A., R.M.K. and N.M.A.-H.; writing—original draft preparation, E.M.B., M.A.S., M.M.D., A.M.A., R.M.K. and N.M.A.-H.; writing—review and editing, E.M.B., M.A.S., M.M.D., A.M.A., R.M.K. and N.M.A.-H.; visualization, E.M.B., N.M.A.-H.; supervision, N.M.A.-H., E.M.B.; project administration, E.M.B., M.A.S. and M.M.D.; funding acquisition, E.M.B. All authors have read and agreed to the published version of the manuscript.

Funding: This work was funded by the Deanship of Scientific Research (DSR) at King Abdulaziz University, Jeddah, Saudi Arabia, under grant no. RG-38-135-42.

Institutional Review Board Statement: Not applicable.

Informed Consent Statement: Not applicable.

Data Availability Statement: Not applicable.

Acknowledgments: This work was funded by the Deanship of Scientific Research (DSR) at King Abdulaziz University, Jeddah, Saudi Arabia, under grant no. RG-38-135-42. The authors, therefore, gratefully acknowledge DSR's technical and financial support.

Conflicts of Interest: The authors declare no conflict of interest.

References

1. Danjumma, S.G.; Abubakar, Y.; Suleiman, S. Nickel oxide (NiO) devices and applications: A review. *J. Eng. Res. Technol.* **2019**, *8*, 12–21.
2. Yakuphanoglu, F. Synthesis and electro-optic properties of nanosized-boron doped cadmium oxide thin films for solar cell applications. *Sol. Energy* **2011**, *85*, 2704–2709. [[CrossRef](#)]
3. Fan, L.; Zhu, B.; Chen, M.; Wang, C.; Raza, R.; Qin, H.; Wang, X.; Wang, X.; Ma, Y. High performance transition metal oxide composite cathode for low temperature solid oxide fuel cells. *J. Power Sources* **2012**, *203*, 65–71. [[CrossRef](#)]
4. Atchuta, S.; Sakthivel, S.; Barshilia, H.C. Transition metal based $Cu_xNi_yCo_z-x-yO_4$ spinel composite solar selective absorber coatings for concentrated solar thermal applications. *Sol. Energy Mater. Sol. Cells* **2019**, *189*, 226–232. [[CrossRef](#)]
5. Yu, X.; Qu, B.; Zhao, Y.; Li, C.; Chen, Y.; Sun, C.; Gao, P.; Zhu, C. Growth of hollow transition metal (Fe, Co, Ni) oxide nanoparticles on graphene sheets through Kirkendall effect as anodes for high-performance lithium-ion batteries. *Chem. A Eur. J.* **2016**, *22*, 1638–1645. [[CrossRef](#)]
6. Absi, E.; Saleh, M.; Al-Hada, N.M.; Hamzah, K.; Alhawsawi, A.M.; Banoqitah, E.M. A review on preparation and characterization of silver/nickel oxide nanostructures and their applications. *Appl. Phys. A* **2021**, *127*, 1–32.
7. El Sayed, A.; El-Sayed, S.; Morsi, W.; Mahrous, S.; Hassen, A. Synthesis, characterization, optical, and dielectric properties of polyvinyl chloride/cadmium oxide nanocomposite films. *Polym. Compos.* **2014**, *35*, 1842–1851. [[CrossRef](#)]

8. Aldeen, T.S.; Mohamed, H.E.A.; Maaza, M. Bio-inspired Single Phase Montepionite CdO Nanoparticles via Natural Extract of Phoenix roebelenii Palm Leaves. *J. Inorg. Organomet. Polym. Mate-Rials* **2020**, *30*, 4691–4701. [[CrossRef](#)]
9. Al-Hada, N.M.; Saion, E.B.; Shaari, A.H.; Kamarudin, M.A.; Flaifel, M.H.; Ahmad, S.H.; Gene, A. A facile thermal-treatment route to synthesize the semiconductor CdO nanoparticles and effect of calcination. *Mate-Rials Sci. Semicond. Process.* **2014**, *26*, 460–466. [[CrossRef](#)]
10. Sakthivel, P.; Murugan, R.; Asaithambi, S.; Karuppaiah, M.; Vijayaprasath, G.; Rajendran, S.; Hayakawa, Y.; Ravi, G. Radio frequency power induced changes of structural, morphological, optical and electrical proper-ties of sputtered cadmium oxide thin films. *Thin Solid Film.* **2018**, *654*, 85–92. [[CrossRef](#)]
11. Haacke, G. Transparent conducting coatings. *Annu. Rev. Mater. Sci.* **1977**, *7*, 73–93. [[CrossRef](#)]
12. Balamurugan, S.; Balu, A.; Usharani, K.; Suganya, M.; Anitha, S.; Prabha, D.; Ilangoan, S. Synthesis of CdO nanopowders by a simple soft chemical method and evaluation of their antimicrobial activities. *Pac. Sci. Rev. A Nat. Sci. Eng.* **2016**, *18*, 228–232. [[CrossRef](#)]
13. Kaviyarasu, K.; Manikandan, E.; Paulraj, P.; Mohamed, S.B.; Kennedy, J. One dimensional well-aligned CdO nanocrystal by solvothermal method. *J. Alloys Compd.* **2014**, *593*, 67–70. [[CrossRef](#)]
14. Karmakar, S.; Raviteja, B.; Mistari, C.D.; Parey, V.; Thapa, R.; More, M.; Behera, D. Superior field emission and alternating current conduction mechanisms for grains and grain boundaries in an NiO-[CdO]₂ nano-composite. *J. Phys. Chem. Solids* **2020**, *142*, 109462. [[CrossRef](#)]
15. Shi, M.; Qiu, T.; Tang, B.; Zhang, G.; Yao, R.; Xu, W.; Chen, J.; Fu, X.; Ning, H.; Peng, J. Tempera-ture-Controlled crystallite size of Wide Band Gap Nickel Oxide and Its Application in Electrochromism. *Micromachines* **2021**, *12*, 80. [[CrossRef](#)] [[PubMed](#)]
16. Wang, G.; Zheng, J.; Xu, B.; Zhang, C.; Zhu, Y.; Fang, Z.; Yang, Z.; Shang, M.-H.; Yang, W. Tailored Electronic Band Gap and Valance Band Edge of Nickel Oxide via p-Type Incorporation. *J. Phys. Chem. C* **2021**, *125*, 7495–7501. [[CrossRef](#)]
17. Irwin, M.D.; Buchholz, D.B.; Hains, A.W.; Chang, R.P.; Marks, T.J. p-Type semiconducting nickel oxide as an efficiency-enhancing anode interfacial layer in polymer bulk-heterojunction solar cells. *Proc. Natl. Acad. Sci. USA* **2008**, *105*, 2783–2787. [[CrossRef](#)]
18. Wang, K.-C.; Jeng, J.-Y.; Shen, P.-S.; Chang, Y.-C.; Diao, E.W.-G.; Tsai, C.-H.; Chao, T.-Y.; Hsu, H.-C.; Lin, P.-Y.; Chen, P. P-type mesoscopic nickel oxide/organometallic perovskite heterojunction solar cells. *Sci. Rep.* **2014**, *4*, 4756. [[CrossRef](#)]
19. Dubey, P.; Kaurav, N.; Devan, R.S.; Okram, G.; Kuo, Y. The effect of stoichiometry on the structural, thermal and electronic properties of thermally decomposed nickel oxide. *RSC Adv.* **2018**, *8*, 5882–5890. [[CrossRef](#)]
20. Napari, M.; Huq, T.N.; Hoye, R.L.; MacManus-Driscoll, J.L. Nickel oxide thin films grown by chemical deposition techniques: Potential and challenges in next-generation rigid and flexible device applications. *InfoMat* **2021**, *3*, 536–576. [[CrossRef](#)]
21. Hashem, M.; Saion, E.; Al-Hada, N.M.; Kamari, H.M.; Shaari, A.H.; Talib, Z.A.; Paiman, S.B.; Kamarudeen, M.A. Fabrication and characterization of semiconductor nickel oxide (NiO) nanoparticles manufactured using a facile thermal treatment. *Results Phys.* **2016**, *6*, 1024–1030. [[CrossRef](#)]
22. Liu, A.; Meng, Y.; Zhu, H.; Noh, Y.-Y.; Liu, G.; Shan, F. Electrospun p-type nickel oxide semiconducting nanowires for low-voltage field-effect transistors. *ACS Appl. Mater. Interfaces* **2017**, *10*, 25841–25849. [[CrossRef](#)] [[PubMed](#)]
23. Ponnusamy, P.; Agilan, S.; Muthukumarasamy, N.; Senthil, T.; Rajesh, G.; Venkatraman, M.; Velauthapillai, D. Structural, optical and magnetic properties of undoped NiO and Fe-doped NiO nanoparticles synthe-sized by wet-chemical process. *Mater. Charact.* **2016**, *114*, 166–171. [[CrossRef](#)]
24. Ibrahim, M. Application of Graphene/Nickel Oxide Composite as a Humidity Sensor. *Egypt. J. Chem.* **2021**, *64*, 3–4. [[CrossRef](#)]
25. Munawar, T.; Iqbal, F.; Yasmeen, S.; Mahmood, K.; Hussain, A. Multi metal oxide NiO-CdO-ZnO nanocom-posite-synthesis, structural, optical, electrical properties and enhanced sunlight driven photocatalytic activ-ity. *Ceram. Int.* **2020**, *46*, 2421–2437. [[CrossRef](#)]
26. Sanchez, C.; Belleville, P.; Popall, M.; Nicole, L. Applications of advanced hybrid organic-inorganic nano-materials: From laboratory to market. *Chem. Soc. Rev.* **2011**, *40*, 696–753. [[CrossRef](#)]
27. Pal, K.; Si, A.; El-Sayyad, G.S.; Elkodous, M.A.; Kumar, R.; El-Batal, A.I.; Kralj, S.; Thomas, S. Cutting edge development on graphene derivatives modified by liquid crystal and CdS/TiO₂ hybrid matrix: Optoelectronics and biotechnological aspects. *Crit. Rev. Solid State Mater. Sci.* **2020**, *46*, 385–449. [[CrossRef](#)]
28. Elemike, E.E.; Onwudiwe, D.C.; Wei, L.; Chaogang, L.; Zhiwei, Z. Noble metal-semiconductor nanocompo-sites for optical, energy and electronics applications. *Sol. Energy Mater. Sol. Cells* **2019**, *201*, 110106. [[CrossRef](#)]
29. Yasmeen, S.; Iqbal, F.; Munawar, T.; Nawaz, M.A.; Asghar, M.; Hussain, A. Synthesis, structural and optical analysis of surfactant assisted ZnO-NiO nanocomposites prepared by homogeneous precipitation method. *Ceram. Int.* **2019**, *45*, 17859–17873. [[CrossRef](#)]
30. Absi, E.; Saleh, M.A.; Al-Hada, N.M.; Hamzah, K.; Alhawsawi, A.M.; Banoqitah, E.M. Binary nickel and silver oxides by thermal route: Preparation and characterization. *Appl. Phys. A* **2021**, *127*, 606. [[CrossRef](#)]
31. Al-Hada, N.M.; Kamari, H.M.; Abdullah, C.A.C.; Saion, E.; Shaari, A.H.; Talib, Z.A.; Matori, K.A. Down-top nanofabrication of binary (CdO)_x(ZnO)_{1-x} nanoparticles and their antibacterial activity. *Int. J. Nanomed.* **2017**, *12*, 8309. [[CrossRef](#)] [[PubMed](#)]
32. Al-Hada, N.M.; Kamari, H.M.; Shaari, A.H.; Saion, E. Fabrication and characterization of Manganese-Zinc Ferrite nanoparticles produced utilizing heat treatment technique. *Results Phys.* **2019**, *12*, 1821–1825. [[CrossRef](#)]
33. Al-Hada, N.M.; Saion, E.; Kamari, H.M.; Flaifel, M.H.; Shaari, A.H.; Talib, Z.A.; Abdullahi, N.; Baqer, A.A.; Kharazmi, A. Structural, morphological and optical behaviour of PVP capped binary (ZnO) 0.4 (CdO) 0.6 nanoparticles synthesised by a facile thermal route. *Mater. Sci. Semicond. Process.* **2016**, *53*, 56–65. [[CrossRef](#)]
34. Baqer, A.A.; Matori, K.A.; Al-Hada, N.M.; Shaari, A.H.; Saion, E.; Chyi, J.L.Y. Effect of polyvinylpyrrolidone on cerium oxide nanoparticle characteristics prepared by a facile heat treatment technique. *Results Phys.* **2017**, *7*, 611–619. [[CrossRef](#)]

35. Muhamad, S.; Kamari, H.M.; Al-Hada, N.M.; Abdullah, C.A.C.; Nidzam, N.N.S. Fabrication of binary $(\text{ZnO})_x(\text{TiO}_2)_{1-x}$ nanoparticles via thermal treatment route and evaluating the impact of various molar concentrations on the structure and optical behaviors. *Appl. Phys. A* **2020**, *126*, 1–15. [[CrossRef](#)]
36. Al-Hada, N.M.; Saion, E.; Talib, Z.A.; Shaari, A.H. The impact of polyvinylpyrrolidone on properties of cadmium oxide semiconductor nanoparticles manufactured by heat treatment technique. *Polymers* **2016**, *8*, 113. [[CrossRef](#)]
37. Al-Hada, N.M.; Saion, E.B.; Shaari, A.H.; Kamarudin, M.A.; Flaifel, M.H.; Ahmad, S.H.; Gene, S.A. A Facile Thermal-Treatment Route to Synthesize ZnO Nanosheets and Effect of Calcination Temperature. *PLoS ONE* **2014**, *9*, e103134. [[CrossRef](#)]
38. Amani-Beni, Z.; Nezamzadeh-Ejhi, A. NiO nanoparticles modified carbon paste electrode as a novel sulfasalazine sensor. *Anal. Chim. Acta* **2018**, *1031*, 47–59. [[CrossRef](#)]
39. Reddy, C.V.; Babu, B.; Shim, J. Synthesis, optical properties and efficient photocatalytic activity of CdO/ZnO hybrid nanocomposite. *J. Phys. Chem. Solids* **2018**, *112*, 20–28. [[CrossRef](#)]
40. Zeid, E.F.A.; Ibrahim, I.A.; Ali, A.M.; Mohamed, W.A. The effect of CdO content on the crystal structure, surface morphology, optical properties and photocatalytic efficiency of p-NiO/n-CdO nanocomposite. *Results Phys.* **2019**, *12*, 562–570. [[CrossRef](#)]
41. Al-Hada, N.M.; Kasim, H.; Al-Ghaili, A.M.; Saleh, M.A.; Banoqitah, E.M.; Alhawsawi, A.M.; Baqer, A.A.; Liu, J.; Xu, S.; Li, Q. The Effect of Precursor Concentration on the Particle Size, Crystallite Size, and Optical Energy Gap of $\text{Ce}_x\text{Sn}_{1-x}\text{O}_2$ Nanofabrication. *Nanomaterials* **2021**, *11*, 2143. [[CrossRef](#)] [[PubMed](#)]
42. Al-Hada, N.M.; Al-Ghaili, A.M.; Kasim, H.; Saleh, M.A.; Baqiah, H.; Liu, J.; Wang, J. Nanofabrication of $(\text{Cr}_2\text{O}_3)_x(\text{NiO})_{1-x}$ and the impact of precursor concentrations on nanoparticles conduct. *J. Mater. Res. Technol.* **2021**, *11*, 252–263. [[CrossRef](#)]
43. Baqer, A.A.; Matori, K.A.; Al-Hada, N.M.; Shaari, A.H.; Kamari, H.M.; Saion, E.; Chyi, J.L.Y.; Abdullah, C.A.C. Synthesis and characterization of binary $(\text{CuO})_{0.6}(\text{CeO}_2)_{0.4}$ nanoparticles via a simple heat treatment method. *Results Phys.* **2018**, *9*, 471–478. [[CrossRef](#)]
44. Dihom, M.M.; Shaari, A.H.; Baqiah, H.; Al-Hada, N.M.; Kien, C.S.; Azis, R.S.; Kechik, M.M.A.; Talib, Z.A.; Abd-Shukor, R. Microstructure and superconducting properties of Ca substituted $\text{Y}(\text{Ba}_{1-x}\text{Ca}_x)_2\text{Cu}_3\text{O}_{7-\delta}$ ceramics prepared by thermal treatment method. *Results Phys.* **2017**, *7*, 407–412. [[CrossRef](#)]
45. Al-Hada, N.M.; Al-Ghaili, A.M.; Kasim, H.; Saleh, M.A.; Flaifel, M.H.; Kamari, H.M.; Baqiah, H.; Liu, J.; Jihua, W. The Effect of PVP Concentration on Particle Size, Morphological and Optical Properties of Cassiterite Nanoparticles. *IEEE Access* **2020**, *8*, 93444–93454. [[CrossRef](#)]
46. Baqer, A.A.; Matori, K.A.; Al-Hada, N.M.; Kamari, H.M.; Shaari, A.H.; Saion, E.; Chyi, J.L.Y. Copper oxide nanoparticles synthesized by a heat treatment approach with structural, morphological and optical characteristics. *J. Mater. Sci. Mater. Electron.* **2018**, *29*, 1025–1033. [[CrossRef](#)]
47. Zakiyah, L.B.; Saion, E.; Al-Hada, N.M.; Gharibshahi, E.; Salem, A.; Soltani, N.; Gene, S. Up-scalable synthesis of size-controlled copper ferrite nanocrystals by thermal treatment method. *Mater. Sci. Semicon-Ductor Process.* **2015**, *40*, 564–569. [[CrossRef](#)]
48. Morales, A.E.; Mora, E.S.; Pal, U. Use of diffuse reflectance spectroscopy for optical characterization of un-supported nanostructures. *Rev. Mex. De Fis. S* **2007**, *53*, 18.
49. Torrent, J.; Barr'ón, V. *Encyclopedia of Surface and Colloid Science*; Marcel Dekker Inc.: New York, NY, USA, 2002.

Disclaimer/Publisher's Note: The statements, opinions and data contained in all publications are solely those of the individual author(s) and contributor(s) and not of MDPI and/or the editor(s). MDPI and/or the editor(s) disclaim responsibility for any injury to people or property resulting from any ideas, methods, instructions or products referred to in the content.